Available online at www.sciencedirect.com
ScienceDirect
Trans. Nonferrous Met. Soc. China 35(2025) 1456−1470
Transactions of Nonferrous Metals Society of China
www.tnmsc.cn

Static recrystallization kinetics and texture evolution of low-temperature extruded Mg−Zn−Ca alloy during annealing

Hua WANG[1,2], Da-tong ZHANG[1], Cheng QIU[1], Dao-lun CHEN[2]

1. Guangdong Key Laboratory for Advanced Metallic Materials Processing and Forming, National Engineering Research Center of Near-net-shape Forming for Metallic Materials, South China University of Technology, Guangzhou 510640, China;
2. Department of Mechanical, Industrial and Mechatronics Engineering, Toronto Metropolitan University, Toronto, Ontario M5B 2K3, Canada

Received 31 August 2023; accepted 13 May 2024

Abstract: A low-alloyed Mg−1.2Zn−0.1Ca alloy was extruded at 150 °C, followed by annealing at varying temperatures of 200−300 °C. The microstructural evolution and static recrystallization kinetics were investigated. The as-extruded alloy exhibited a bimodal structure consisting of fine recrystallized grains of 0.8 μm and coarse un-recrystallized grains, with a recrystallized fraction of ~67%. The recrystallization process at 250 °C was identified to be appropriate with a slow recrystallized grain growth rate. The grains with $\langle 20\bar{2}1\rangle$, $\langle 20\bar{2}3\rangle$, $\langle \bar{1}2\,\bar{1}2\rangle$ and $\langle \bar{2}7\bar{5}0\rangle$ orientations exhibited preferential growth advantages during long-term annealing. Grain boundary segregation exerted a strong Zener pinning effect on the grain boundaries, which not only increased the grain growth activation energy, but also affected the texture evolution.

Key words: Mg−Zn−Ca alloy; annealing; texture; grain growth; static recrystallization kinetics

1 Introduction

Magnesium (Mg) alloys possess many advantages, such as low density, excellent specific strength and specific stiffness, good damping performance and superior biocompatibility [1,2]. Therefore, Mg alloys have great potential in lightweight applications in the automotive and aerospace, and biomedical fields. Plastic deformation techniques have been widely reported to be an effective method to improve the mechanical properties of Mg alloys [3−5]. However, the hexagonal close-packed (hcp) structure of Mg leads to the formation of strong basal texture with most grains in hard orientations, e.g., basal planes parallel to the extrusion direction (ED) and rolling direction (RD) for extruded and rolled Mg alloys, respectively, which contributes to attaining a high yield strength but decreasing the room-temperature ductility and formability [3,6]. It is reported that Mg alloys with high formability usually exhibit a low yield strength of 100−170 MPa [7]. Therefore, overcoming strength-ductility/formability trade-off becomes a big challenge to fabricate Mg alloys with excellent comprehensive properties. Texture is one of the most important factors which influences the room-temperature ductility and formability of Mg alloys [6,8]. Therefore, tailoring the texture is an essential effort for Mg alloys to achieve superior strength and ductility/formability simultaneously.

The addition of rare-earth (RE) elements has

Corresponding author: Da-tong ZHANG, Tel: +86-20-87112272, E-mail: dtzhang@scut.edu.cn;
Dao-lun CHEN, Tel: +416-979-5000 ext. 556487, E-mail: dchen@torontomu.ca
https://doi.org/10.1016/S1003-6326(24)66760-9

been reported as a viable strategy for weakening the texture of Mg alloys. LI et al [9] reported that pure Mg alloying with element ytterbium (Yb) could promote the formation of ED-tilted texture in extruded Mg alloys. The texture modification by adding RE elements is usually attributed to facilitating the initiation of non-basal slip systems and altering the grain boundary energy and mobility [9,10]. However, alloying with RE elements increases the production cost of Mg alloys. Similar to RE elements, researchers found that the addition of Ca could act as a texture weakening element [11], and RE texture can also be observed in Zn- and Ca-containing Mg alloys, especially alloying with a low content [12,13]. Besides excellent bio-compatibility [14], superior mechanical properties can also be achieved in Mg−Zn−Ca alloys. DU et al [15] reported a high yield strength of 406 MPa in an extruded Mg−2Zn−1.2Ca alloy. Compared with Mg−1.5Zn alloy with an Erichsen value (index of forming quality) of 3.4, CHINO et al [11] reported that a high Erichsen value of 8.2 was obtained in Mg−1.5Zn−0.1Ca alloy prepared by rolling and annealing, due to the splitting of basal planes toward the transverse direction (TD).

Extrusion followed by annealing process is widely used to tailor the microstructure of Mg alloys for acquiring superior performance. WANG et al [16] fabricated a Mg−1.0Bi−1.0Mn−1.0Al−0.5Ca−0.3Zn alloy via extrusion at 300 °C with a speed of 0.5 mm/s, which showed an excellent yield strength of 425 MPa but a low elongation of 2.1%. After annealing at 380 °C for 15 min, balanced tensile properties with a high yield strength of 378 MPa and a good elongation of 16.8% were achieved simultaneously. It is widely reported that a superior strength can be achieved in Mg alloys via decreasing extrusion temperature. In this case, the microstructure is composed of fine dynamic recrystallization (DRX) grains and coarse unDRXed grains [3,16,17]. During annealing, the grains are easy to grow up [18]. Therefore, appropriate annealing parameters are essential for the preparation of high-performance Mg alloys. Besides, static recrystallization (SRX) can occur during annealing in Mg alloys with unDRXed grains, which provides an effective method for weakening the overall texture. Previous studies showed that $\langle 10\bar{1}0\rangle$ [3,19,20], $\langle 10\bar{1}0\rangle - \langle 11\bar{2}0\rangle$ [9,19], $\langle 11\bar{2}0\rangle$ [19,20] and RE (e.g. $\langle 11\bar{2}1\rangle$ and $\langle 11\bar{2}2\rangle$) [20,21] texture components parallel to ED can be formed in extruded Mg alloys. After annealing, new texture components may occur [9,13]. CANO-CASTILLO et al [13] reported that $\langle 10\bar{1}0\rangle$ texture component transformed into $\langle 20\bar{2}1\rangle$ texture in a Mg−0.94Zn−0.15Ca alloy after annealing. Such a transition of texture provides potential for regulating the mechanical properties of Mg alloys.

Our previous work demonstrated that a superior yield strength of 374 MPa was achieved in a low-alloyed Mg−1.2Zn−0.1Ca alloy with a partially-DRXed microstructure via extrusion at 150 °C [22]. However, a strong basal texture was formed. Also, strain softening occurred during the subsequent tensile deformation, like other studies [3]. In the present study, different annealing temperatures were adopted to treat the low-temperature extruded Mg−1.2Zn−0.1Ca alloy. The aim was to investigate the microstructural evolution and SRX kinetic behavior, and provide a theoretical support for the performance regulation of the low-temperature extruded alloy.

2 Experimental

The as-cast Mg−1.2Zn−0.1Ca (wt.%) alloy was homogenized at 375 °C for 24 h and then extruded at 150 °C with an extrusion ratio of 17.4:1 and a ram speed of ~2 mm/s. Subsequently, the extruded bar was subjected to annealing at varying temperatures (100, 150, 200, 250, and 300 °C) for different time (0.5−3600 min). After annealing treatment, the samples were cooled in water. For the sake of convenience, the annealed samples were labeled in the form of annealing temperature−annealing time. For example, the sample annealed at 250 °C for 30 min was labeled as 250 °C−30 min.

Optical microscopy (OM, Keyence, VHX−600, Osaka, Japan) and scanning electron microscope (SEM, Nova NanoSEM430, FEI, Hillsboro, OR, USA) were applied to observing the microstructure of the as-extruded and annealed samples. The RX fraction was determined via ImageJ software. Electron backscatter diffraction (EBSD, C-Nano, Oxford Instruments, UK) in a scanning electron microscope (SEM, Gemini 300, Zeiss, Germany) was used to characterize grain orientations. The EBSD data were analyzed via Channel 5 software. Transmission electron microscopy (TEM, Talos

F200X, FEI, USA) with energy dispersive X-ray spectroscopy (EDS) was used to observe fine precipitates and crystal defects of the annealed samples. Hardness was measured with HVS−1000 Vickers microhardness tester at a load of 100 g and a dwell time of 10 s.

3 Results

3.1 Microstructure

Figure 1 shows the microstructures of the as-cast, homogenized and extruded samples. The as-cast alloy has a coarse grain size of ~170 μm measured by the linear intercept method (Fig. 1(a)). Besides, some secondary-phase particles can be observed in the inserted SEM image, as marked by red arrows. Our previous studies [8,22] revealed that these particles were rich in Mg, Zn and Ca elements, verifying their composition as $Ca_2Mg_6Zn_3$ phase. Homogenization treatment has little effect on the grain size compared with the as-cast alloy (Fig. 1(b)). The inserted SEM image shows that no obvious secondary-phase particles can be observed, indicating that the coarse secondary-phase particles have been basically dissolved into the α-Mg matrix, which facilitates the subsequent low-temperature extrusion. Figures 1(c−e) show that extrusion at 150 °C leads to the occurrence of partial DRX, with a bimodal structure consisting of fine DRX grains and coarse unDRXed grains. At least three regions were used to determine the DRX fraction, with an average value of (67.2±1.7)%. Figure 1(e) shows a band contrast map of the extruded alloy. As indicated by red lines, it is seen that the unDRXed grains consist of numerous low-angle grain boundaries (LAGBs, 2°−15°). The average DRX grain size is measured to be (0.8±0.4) μm based on the EBSD data.

Figures 2(a−h) show the OM images of samples annealed at 200 °C for 30−3600 min. It can be seen that the unRXed regions in the annealed samples can be well maintained for the annealing time shorter than 1080 min. After annealing for 1440 min, a nearly fully-RXed microstructure is obtained, with a RX fraction of (97.7±0.5)%. Further increasing annealing time has little influence on the RX fraction, but would lead to an obvious grain growth. The increased RX fraction indicates that SRX contributes to refining the coarse unRXed grains during annealing. When the annealing temperature increases to 250 °C (Figs. 2(i−o)) and 300 °C (Figs. 2(p−w)), time for achieving nearly fully-RXed structure is significantly shortened with a time of 90 min at 250 °C (Fig. 2(k)) and 3 min at

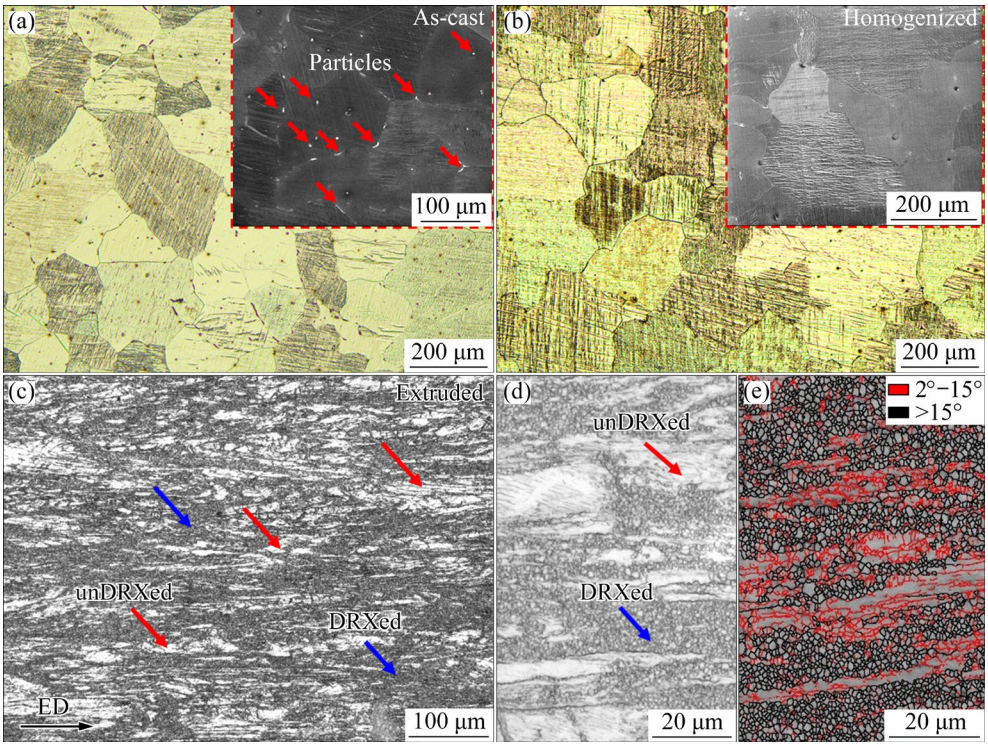

Fig. 1 Microstructures of as-cast (a), homogenized (b) and extruded (c, d) alloys at low magnification (c) and high magnification (d), and band contrast map of extruded alloy (e)

300 °C (Fig. 2(s)), respectively. However, high-temperature annealing gives rise to a significant grain coarsening in a short time.

Figure 3(a) presents the relationships between the RX fraction/average RX grain size and annealing temperature for 30 min with inserted OM images annealed at 100 and 150 °C. It can be seen that annealing below 150 °C can hardly promote the occurrence of SRX, indicating the superior thermo-stability below 150 °C. Figures 3(b−d) display the RX fraction and average RX grain size as a function of annealing time for temperatures ranging from

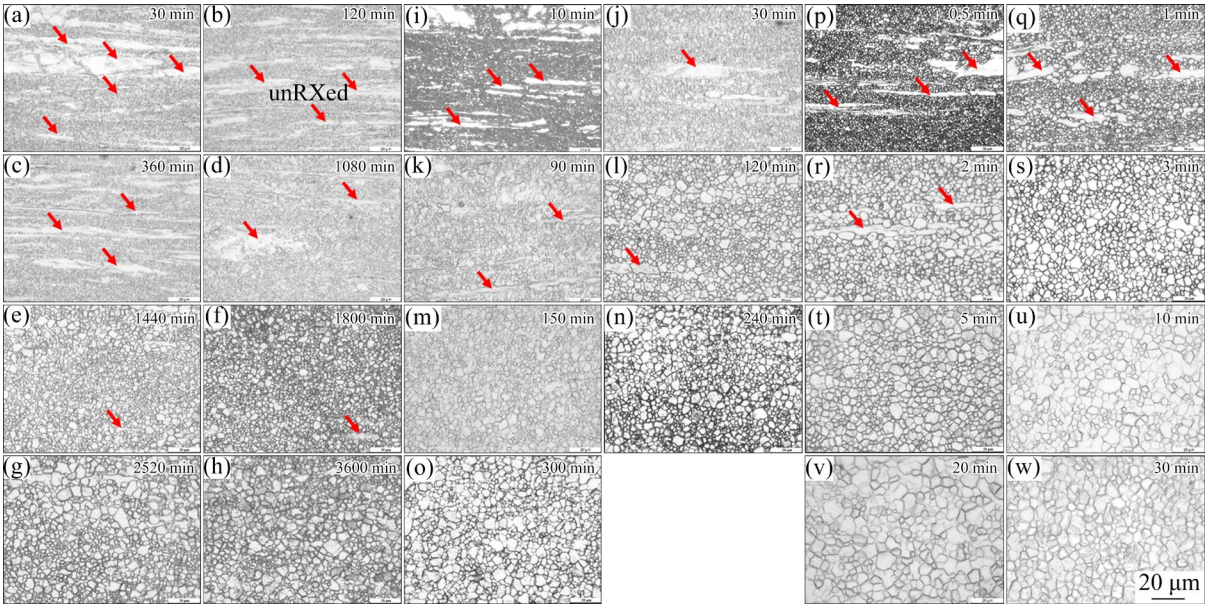

Fig. 2 OM images of samples annealed at 200 °C (a−h), 250 °C (i−o), and 300 °C (p−w)

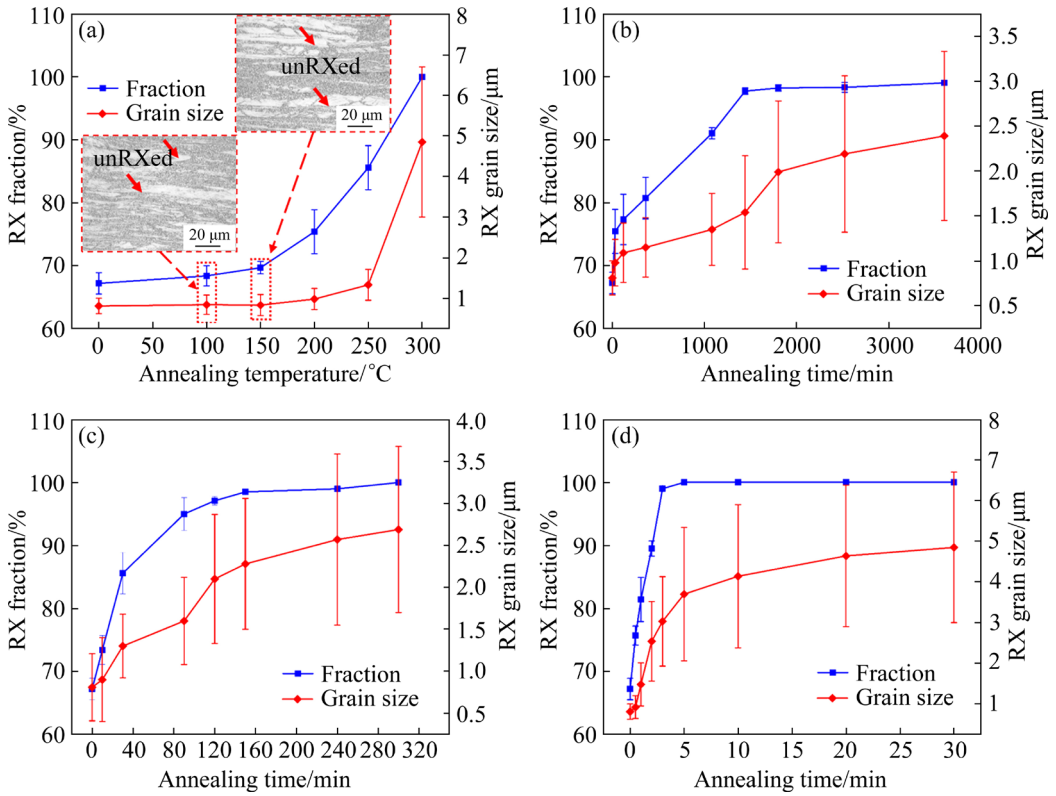

Fig. 3 Relationship between RX fraction/RX grain size and annealing temperature for 30 min with inserted OM images annealed at 100 and 150 °C (a), and relationship between RX fraction/RX grain size and annealing time at different temperatures of 200 °C (b), 250 °C (c) and 300 °C (d)

200 to 300 °C. The results clearly show that the RX fraction gradually increases with increasing annealing time. Moreover, high annealing temperature can accelerate the SRX process and shorten the time for obtaining fully-RXed microstructures. Besides, the average RX grain size also shows an increased trend with increasing time. For samples annealed at 200 °C, the average RX grain size increases from ~1.0 to ~2.4 μm by increasing annealing time from 30 to 3600 min. As to 250 °C, the sample annealed for 90 min has an average RX grain size of ~1.6 μm. Further increasing temperature to 300 °C, the average RX grain size coarsens significantly from ~1.5 to ~4.9 μm with increasing time from 1 to 30 min.

ALIZADEH et al [23] used the term, $(D-D_0)/D_0$, where D and D_0 refer to the current and initial grain size, respectively, to calculate the grain growth factor. Here, to clearly show the RX grain growth rate (f), the following equation is applied:

$$f=\frac{D_i-D_0}{t} \tag{1}$$

where D_i and D_0 represent the average RX grain size of the annealed sample and the as-extruded alloy, respectively, and t is the annealing time. The relationship between the RX grain growth rate and annealing time is shown in Fig. 4. At the early stage of annealing, SRX nucleation occurs in the unRXed grains via the consumption of stored strain energy. As the unRXed grains are gradually replaced by fine SRX grains, the strain energy gradually decreases to a low level. A nearly fully-RXed microstructure is determined by a RX fraction of ≥95%. As shown in Fig. 3, the time to obtain a nearly fully-RXed microstructure at 200, 250 and 300 °C is about 1440, 90 and 3 min, respectively. After that, the growth rate exhibits a decreased trend. It is seen from Fig. 4 that samples annealed at 300 °C exhibit the highest growth rate. For example, at the time attaining nearly fully-RXed microstructure, 300 °C−3 min sample shows a RX grain growth rate of ~0.74 μm/min, which is much higher than that of 200 °C−1440 min (~5.07×10^{-4} μm/min) and 250 °C−90 min (~8.78×10^{-3} μm/min) samples. From the economic perspective as well as for achieving fine-grained microstructure, 250 °C is considered as the best annealing temperature among the three temperatures.

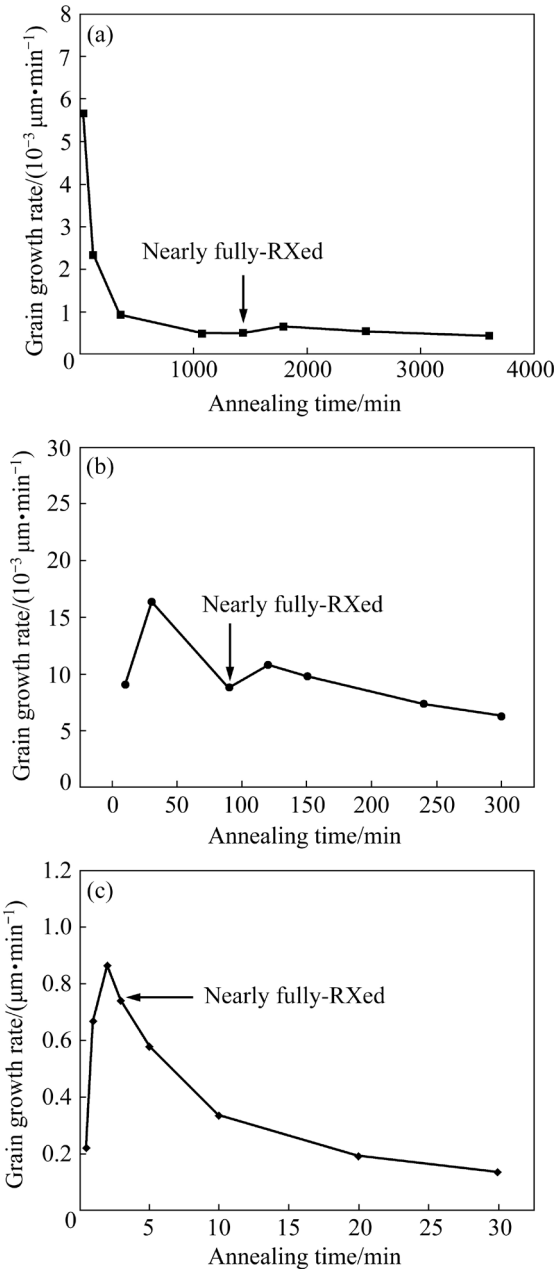

Fig. 4 Relationship between RX grain growth rate and annealing time at different temperatures of 200 °C (a), 250 °C (b), and 300 °C (c)

Figure 5 shows typical SEM and bright-field TEM images of a 250 °C−90 min sample. No obvious coarse secondary phase can be observed in the SEM image (Fig. 5(a)). In the TEM image (Fig. 5(b)), it can be seen that fine precipitates distribute along grain boundaries, which can hinder the grain growth during annealing via Zener pinning (or Zener drag) effect [24,25]. Our previous work revealed that co-segregation of Zn and Ca atoms along grain boundaries existed in the as-extruded alloy [22]. After annealing at 250 °C

for 90 min, co-segregation of Zn and Ca atoms along grain boundaries can also be observed, as shown in Fig. 6.

3.2 Microhardness

Figure 7(a) shows the change of microhardness with the annealing time at different temperatures. The as-extruded alloy has the highest microhardness (HV ~82). After annealing, it can be seen that the microhardness decreases with increasing annealing time, and the decreasing trend is much faster at higher annealing temperatures. A similar change of hardness as a function of annealing time has been reported in rolled Mg−1.6Al−0.8Zn−0.4Mn−0.5Ca alloy [26] and Mg−2Zn based magnesium alloys [27].

Figure 7(b) displays the relationship between the microhardness and the logarithm of annealing

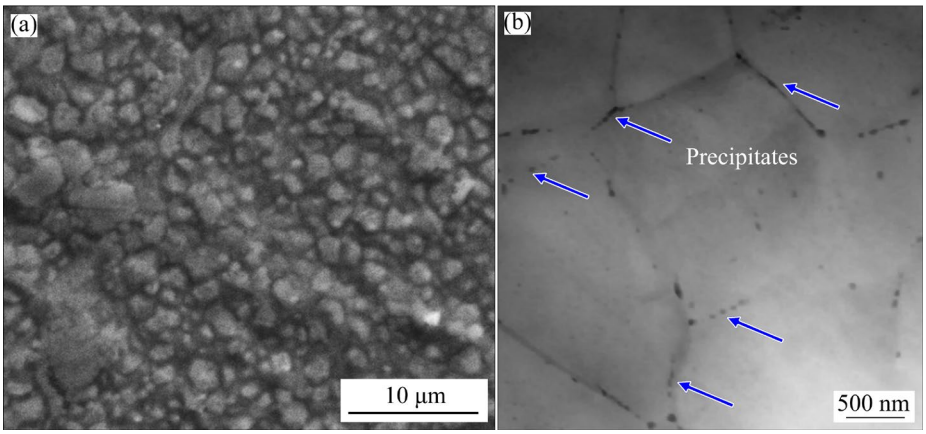

Fig. 5 SEM (a) and bright-field TEM (b) images of 250 °C−90 min sample

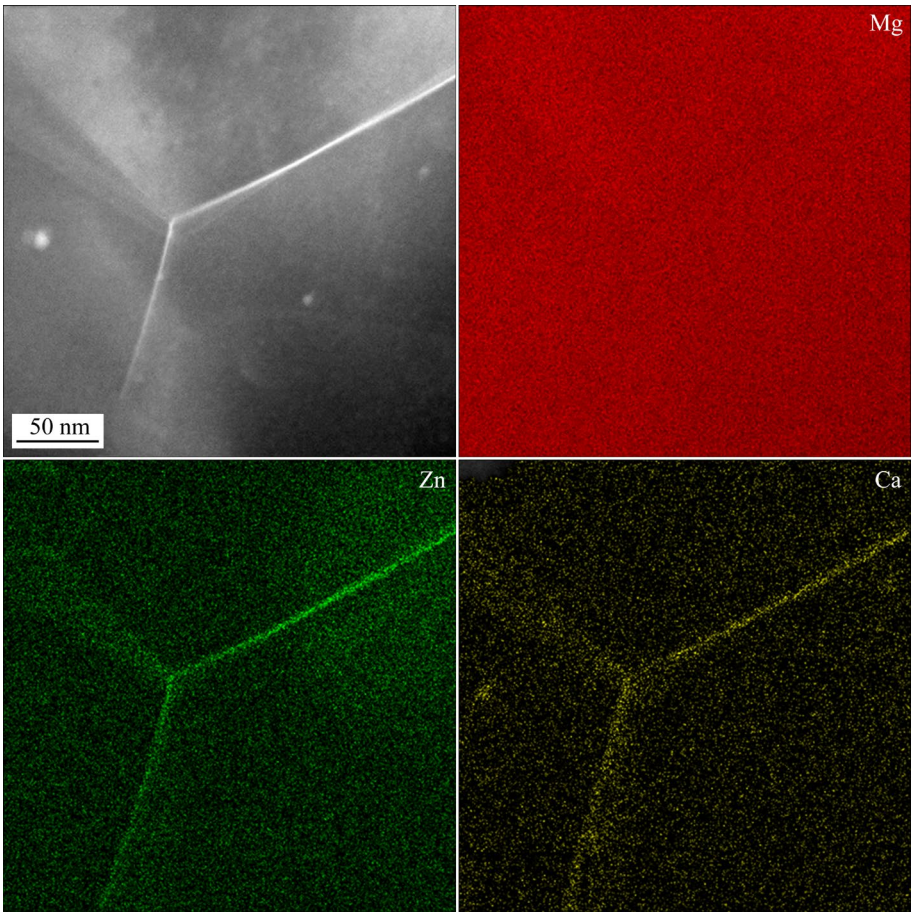

Fig. 6 Elemental distribution showing co-segregation of Zn and Ca elements along grain boundaries in 250 °C−90 min sample

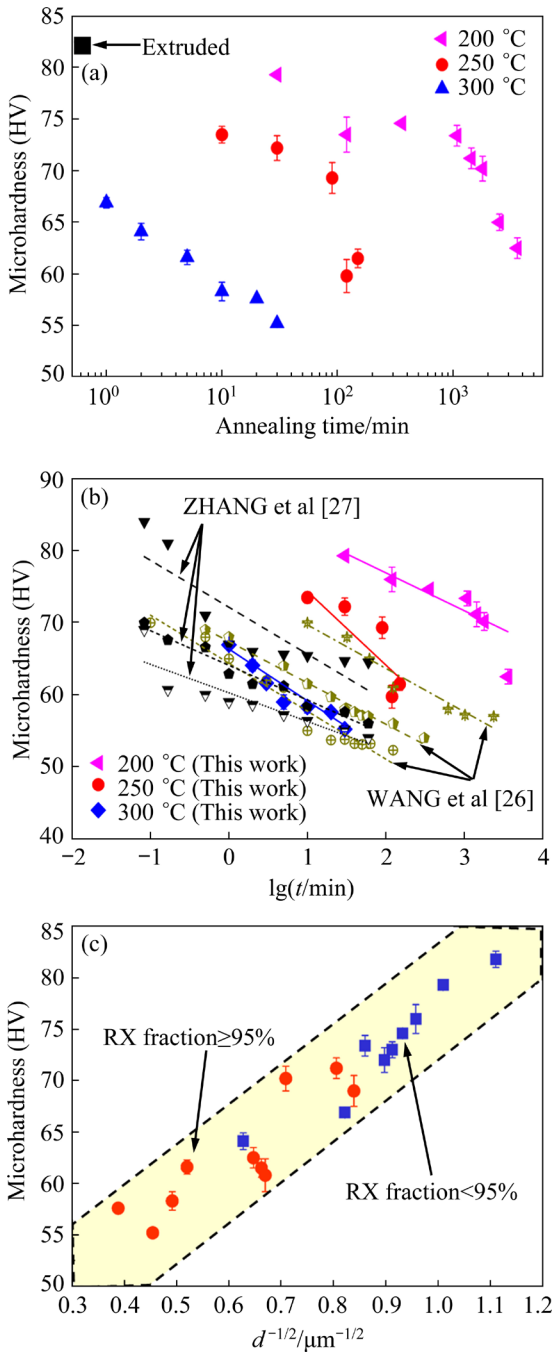

Fig. 7 Relationship between microhardness and annealing time at different temperatures (a), relationship between microhardness and lg t of Mg−1.6Al−0.8Zn−0.4Mn−0.5Ca alloy [26], Mg−2Zn based magnesium alloy [27] and present alloy (b), and plot of microhardness versus $d^{-1/2}$ (c)

time (lg t) of Mg−1.6Al−0.8Zn−0.4Mn−0.5Ca alloy [26], Mg−2Zn based magnesium alloy [27] and the present alloy. It can be seen that the microhardness decreases approximately linearly with lg t.

Figure 7(c) shows the relationship between microhardness and average RX grain size (d). It is seen that the microhardness shows an increased trend with decreasing RX grain size for samples with a RX fraction of ≥95%, which is consistent with other studies [21,28]. Interestingly, most of the microhardness values for samples with a RX fraction of <95% are higher than those of samples with a RX fraction of ≥95%, and also follow the relationship that the microhardness increases with decreasing RX grain size. LIU et al [29] reported that the difference of microhardness between the fine RX grains and coarse unRXed grains was small in an extruded Mg−13Gd alloy (HV 89.6 vs HV 91.5). Besides grain sizes, it can be inferred that other factors could also affect the microhardness. Texture has an important effect on the yield strength, but has little influence on the microhardness [30,31]. It is reported that dislocation density may have an effect beyond grain boundaries, resulting in a nonlinear relationship between the microhardness and grain size [30]. Therefore, the microhardness is controlled by both the quantity of grain boundaries and the density of dislocations.

4 Discussion

4.1 Nucleation and grain growth kinetics during SRX process

Johnson−Mehl−Avrami−Kolmogorov (JMAK) model was usually applied to describing the static recrystallization kinetics. The equation is expressed as follows [32]:

$$X_R=1-\exp(-Bt^n) \quad (2)$$

where X_R, t and B represent the recrystallization fraction, annealing time and factor related to the shape of grains, respectively. To obtain the Avrami exponent value (n), the relationship between $\ln\ln[1/(1-X_R)]$ and $\ln t$ is obtained by natural logarithm transformation as follows:

$$\ln\ln\left(\frac{1}{1-X_R}\right)=\ln B+n\ln t \quad (3)$$

For materials with an initial RX fraction of zero, X_R refers to the RX fraction measured from the microstructure after annealing. However, the present as-extruded alloy has an initial DRX fraction of ~0.67. It is noted that the RX fraction shown in Fig. 3 contains the DRX fraction and SRX

fraction. Thus, the SRX fraction (X_{SRX}) is used here, which can be calculated via the following equation:

$$X_{SRX}=X_{Total\ RX}-X_{DRX} \quad (4)$$

where $X_{Total\ RX}$ is the total RX fraction containing the SRX and DRX fraction, as shown in Fig. 3, and X_{DRX} is the initial DRX fraction of the as-extruded alloy. Figure 8 shows the relationship between $\ln\ln[1/(1-X_{SRX})]$ and $\ln t$. Then, the fitted slope is the value of n, which is 0.37, 0.73 and 0.80 for 200, 250 and 300 °C, respectively. It is noted that the value of n increases with increasing temperature. WANG et al [26] calculated the n value to be 0.68−1.02 after annealing at 200−450 °C in a hot-rolled Mg−1.6Al−0.8Zn−0.4Mn−0.5Ca alloy. CHAO et al [33] reported that the n value was in the range of 1.18−1.38 for a cold-drawn AZ31 alloy annealed at 210−300 °C. The n values in these studies were found to increase with annealing temperature as well, being similar to the results in this work. The result reported by SU et al [34] suggested that a relatively high strain and annealing temperature could result in a high n value (1.5−3.4). A low n value may be related to the non-random RX sites of the deformed grains [34]. During annealing, high energy regions, such as those with secondary-phase particles, twins and grain boundaries, are easy to become the nucleation sites [26,33]. In this work, the content of secondary-phase particles is low in the experimental material since they are dissolved into α-Mg matrix after homogenization. Besides, twins are hardly observed in the unDRXed grains (Figs. 1(c−e)). Therefore, the preferential nucleation sites are the grain boundaries of unDRXed grains [35].

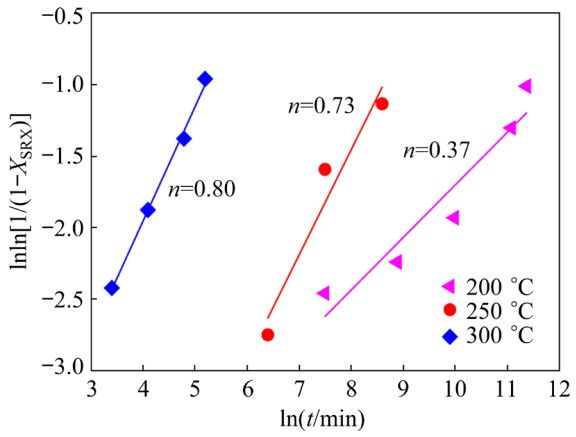

Fig. 8 Plot of $\ln\ln[1/(1-X_{SRX})]$ against $\ln t$ for as-extruded alloy annealed at different temperatures

The grain growth behavior of metallic materials can be described by following equation [36]:

$$D^p-D_0^p=Ct\exp\left(-\frac{Q}{RT}\right) \quad (5)$$

where p, C, t, Q, R and T are grain growth exponent, material constant, annealing time, activation energy for grain growth, molar gas constant and annealing temperature, respectively. This model assumed that the RX grain growth is controlled by grain boundary migration, and the driving force for grain growth is mainly the pressure on grain boundaries.

Another model hypothesized that the grain growth was governed by the difference between the ultimate limiting grain size (D_m) and the instantaneous grain size (D). The corresponding relationship is expressed by [36]

$$\frac{D_0-D}{D_m}+\ln\left(\frac{D_m-D_0}{D_m-D}\right)=\frac{k_0t}{D_m^2}\exp\left(\frac{-Q}{RT}\right) \quad (6)$$

where k_0 is the material constant. Then,

$$\frac{dD}{dt}=k\left(\frac{1}{D}-\frac{1}{D_m}\right) \quad (7)$$

The relationship between dD/dt and $1/D$ is shown in Figs. 9(a−c). The k value is the slope of the linear fitting line, which is 5.2×10^{-5}, 8.5×10^{-4} and 5.0×10^{-2} μm²/s for 200, 250 and 300 °C, respectively, showing an exponentially increasing trend with increasing annealing temperature.

Then, Arrhenius-type equation is used to describe the relationship between the constant (k) and the activation energy of grain growth (Q_G) [36]:

$$k=k_0\exp\left(\frac{-Q_G}{RT}\right) \quad (8)$$

By taking natural logarithm on both sides of Eq. (8), it becomes

$$\ln k=-\frac{Q_G}{RT}+\ln k_0 \quad (9)$$

Figure 9(d) gives the linear fitting between the $\ln k$ and $1/T$ at different annealing temperatures. The value of $-Q_G/R$ is the slope of linear fitting curve. Therefore, the value of Q_G is measured to be ~153 kJ/mol, which is much higher than that for the grain boundary diffusion of Mg (92 kJ/mol) and

slightly higher than that for the lattice self-diffusion

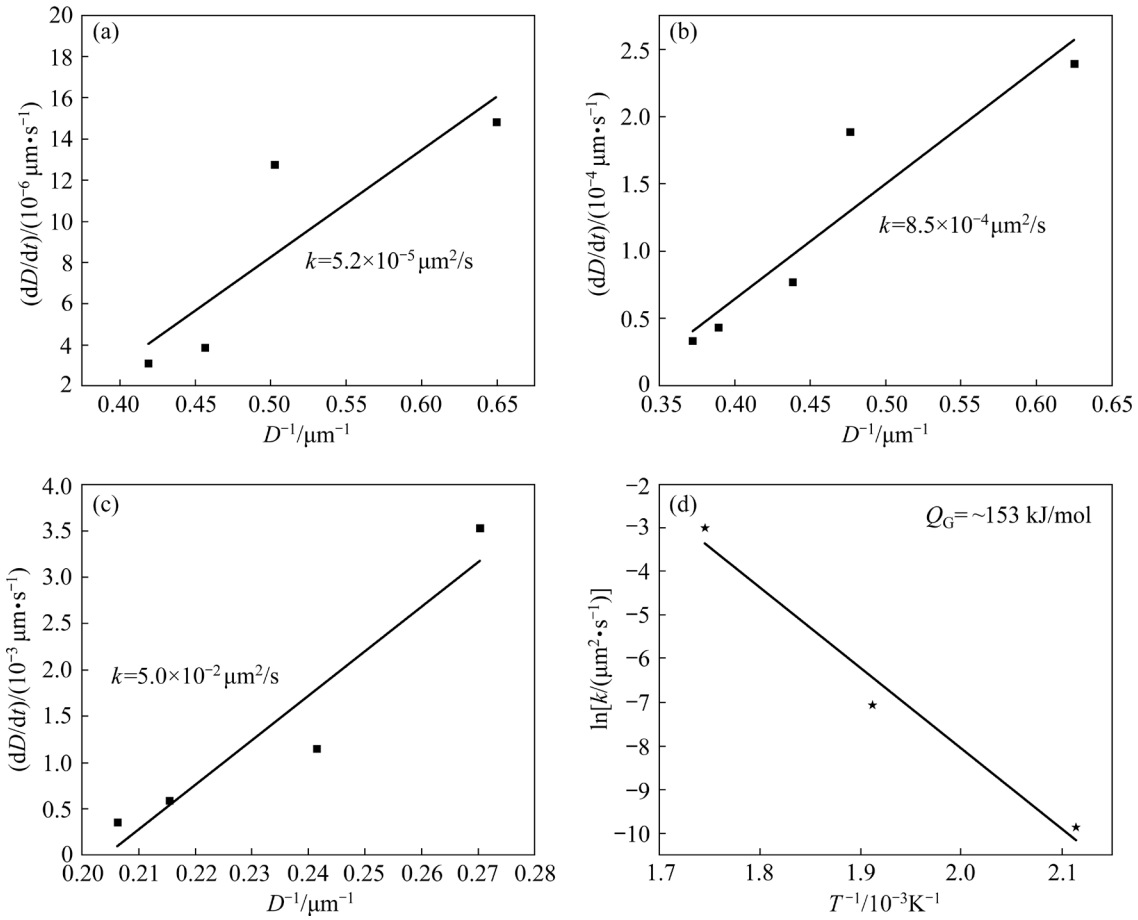

Fig. 9 Plots of dD/dt against 1/D at different temperatures to determine value of k: (a) 200 °C; (b) 250 °C; (c) 300 °C; (d) Plot of ln k against T^{-1} to calculate activation energy for grain growth

of Mg (135 kJ/mol). ALIZADEH et al [23] reported that the Q_G value was ~147 kJ/mol for Mg−Gd−Y−Zr alloy in the temperature range of 400−450 °C. PEI et al [37] reported that the Q_G values were 200 kJ/mol and 269 kJ/mol for Mg−Al−Zn−Ca and Mg−Al−Zn−Ca−Y alloys, respectively. The higher Q_G value was related to the stronger Zener drag and solute drag force to the movement of high-angle grain boundaries. In the present study, grain boundary segregation can be observed (Fig. 5), which decreases the grain boundary energy, thus increasing the stability and hindering the grain growth during annealing [38,39], and resulting in a high activation energy for the grain growth.

4.2 Effect of grain growth on texture evolution

The EBSD orientation maps and the corresponding inverse pole figures in the as-extruded and 250 °C−90 min samples were presented in our previous work, which showed that the main texture component was $\langle 01\bar{1}0\rangle$//ED for both the extruded and 250 °C−90 min samples [40]. The low-annealing temperature and short duration time result in a limited grain size change. The question remains as to what texture forms when the grain size changes greatly.

An experiment was designed to anneal the material at 300 °C for 10 h (300 °C−10 h sample). Figure 10(a) shows the EBSD orientation map with an inserted SEM image of 300 °C−10 h sample, where some coarser RX grains can be observed, as indicated by red arrows. Figure 10(b) presents the grain size distribution of the 300 °C−10 h sample, which shows that the grain sizes are mainly in the range of 5−30 μm, with an average grain size of 13.4 μm. The basal (0001) texture intensity is 2.47 MRD (Fig. 10(c)). Besides, the inverse pole figure clearly shows that four texture components are formed (Fig. 10(d)), including $\langle 20\bar{2}1\rangle$, $\langle 20\bar{2}3\rangle$, $\langle \bar{1}2\bar{1}2\rangle$ and $\langle \bar{2}7\bar{5}0\rangle$, where

$\langle 20\bar{2}1\rangle$ and $\langle 20\bar{2}3\rangle$ components have a higher texture intensity.

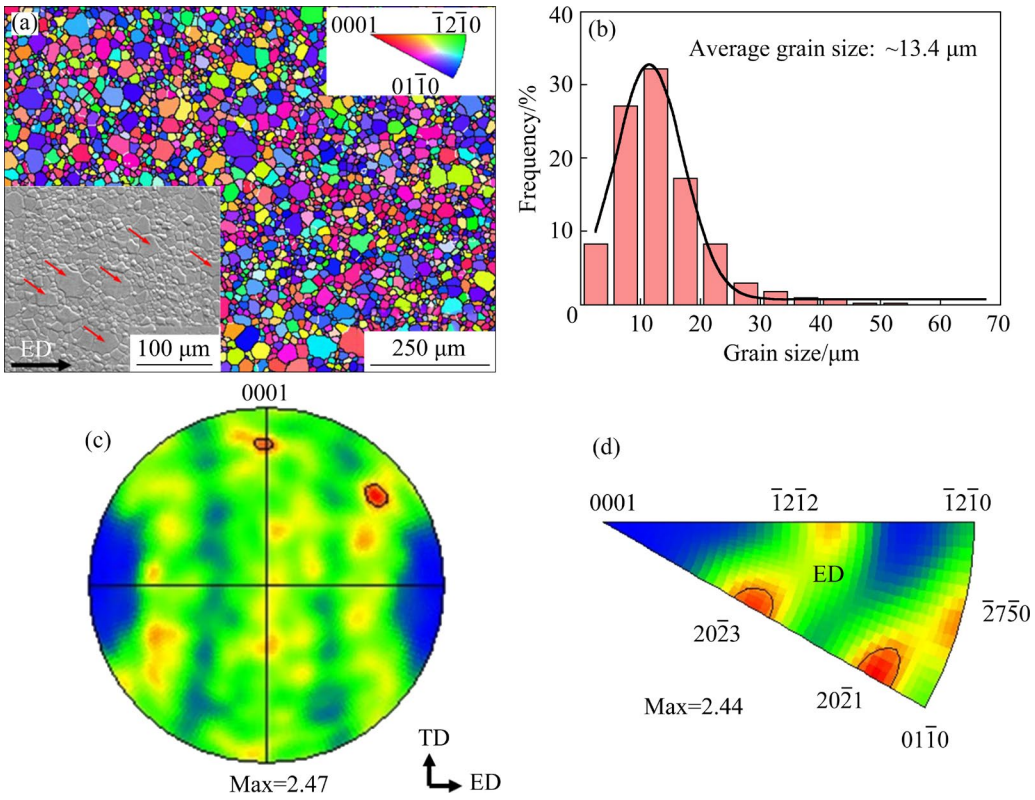

Fig. 10 EBSD orientation map with inserted SEM image of 300 °C−10 h sample (a), corresponding grain size distribution (b), (0001) pole figure (c), and inverse pole figure (d)

During annealing the main change is that SRX nucleation occurs and the fine RX grains of ~0.8 μm in the as-extruded alloy grow to ~13.4 μm in 300 °C−10 h sample. JIANG et al [35] and LIU et al [41] reported that the SRX nucleation showed randomized orientations via quasi-in-situ EBSD method, and exhibited little contribution to the overall texture. Therefore, the reasons for the formed texture components in 300 °C−10 h sample should not be attributed to the SRX nucleation. Preferential grain growth is widely reported to be a main reason for the texture evolution of Mg alloys during annealing [18,35,41]. It is noted that the as-extruded alloy has a higher fraction of $\langle 01\bar{1}0\rangle$-oriented RX grains before annealing [40]. Therefore, the $\langle 01\bar{1}0\rangle$-oriented RX grains are gradually replaced by their adjacent grains during long-term annealing. Factors influencing the grain growth behavior would affect the texture evolution.

Strain energy can provide a driving force for grain growth [18, 42]. VICTORIA-HERNANDEZ et al [42] reported that the grain growth path was towards the region with a higher KAM value via ex-situ EBSD measurements. Therefore, grains with a low strain energy can grow up preferentially by consuming the strain energy of neighbouring grains with a higher strain energy. Due to the strain energy difference between the $\langle 01\bar{1}0\rangle$ and $\langle \bar{1}2\bar{1}1\rangle$ orientations, WU et al [18] reported that preferential grain growth behavior during annealing could lead to the formation of $\langle \bar{1}2\bar{1}1\rangle$ texture at the expense of $\langle 01\bar{1}0\rangle$ texture in an extruded Mg−1Gd alloy. Other researchers [35,41] also reported that $\langle 01\bar{1}0\rangle$-oriented grains had a higher KAM value compared with other orientations, which should be one of the reasons for the transformation of $\langle 01\bar{1}0\rangle$ to other texture components in 300 °C−10 h sample.

Particles and solute atoms can impede grain growth, thus affecting the texture evolution. Figures 11(a, b) show the bright-field TEM images of 300 °C−10 h sample. As indicated by red arrows, precipitates can be observed within the grains. It is expected that these inner precipitates have no effect on hindering the movement of grain boundaries. Grain boundary segregation can act as an important mechanism of fine grains via decreasing grain boundary energy [38,39] and exerting a strong

Zener drag force [24,25]. Segregation can be observed in 250 °C−90 min sample from the bright grain boundaries and EDS elemental maps (Fig. 6). To better show the segregation in 300 °C−10 h sample, different sized grain boundaries were observed in a high-angle annular dark-field (HAADF) imaging mode. In Fig. 11(a), it is seen that the grain boundary is bright in the inserted HAADF image, which confirms the presence of segregation along the grain boundary. The HAADF images in Figs. 11(c) and (d) are magnified from Fig. 11(b), which refer to the boundaries of relatively fine grains. Grain boundary segregation can also be clearly observed from the bright grain boundaries.

GUAN et al [12] reported that segregation occurred in a wide range of grain boundary types in a rolled Mg−0.8Zn−0.2Ca alloy. In a recent work reported by ZHANG et al [43], anisotropic segregation was confirmed in a rolled Mg−2.2Al−0.33Ca alloy, where the growth of basal-oriented grains during annealing was restricted due to the co-segregation of Al and Ca atoms. However, the mechanism driving the preferential segregation to boundaries of basal-oriented grains remains unclear. What becomes evident is that the segregation behavior changes the mobility of grain boundaries, influencing the texture evolution of Mg alloys. JIANG et al [35] inferred that solute atoms preferentially segregated along high-energy basal-oriented grains in a Mg−1.58Zn−0.52Gd alloy, promoting the preferential growth of grains with RE texture orientation and leading to the formation of RE texture after annealing. Segregation is confirmed in 250 °C−90 min (Fig. 6) and 300 °C−10 h (Fig. 11) samples in the present work. Therefore, it is reasonable to infer that the segregation behavior may hinder the growth of $\langle 01\bar{1}0 \rangle$ -oriented grains, and contribute to the formation of the four texture components in the 300 °C−10 h sample.

Specific low-energy grain boundaries are also reported to be the reason for texture evolution [44,45]. Figure 12 shows the correlated (indicated by red histogram) and uncorrelated (indicated by blue line) misorientation angle distributions of the RX region in the as-extruded alloy and 300 °C−10 h sample. The random

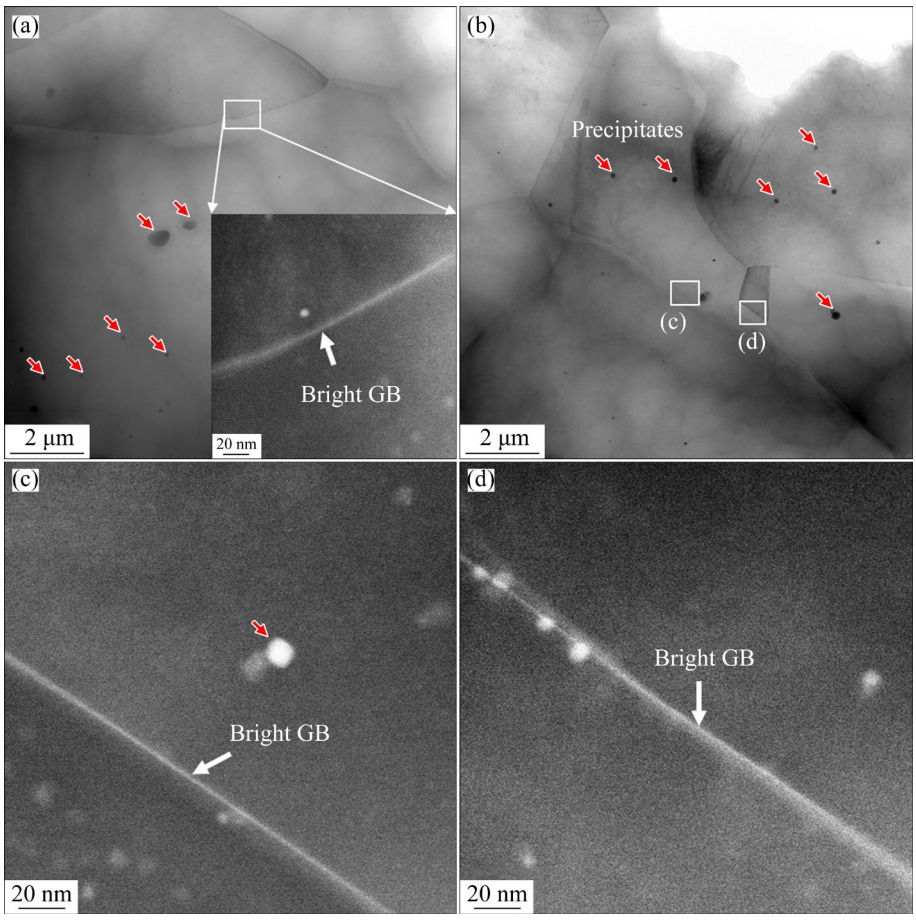

Fig. 11 (a, b) Bright-field TEM images of 300 °C−10 h sample; (c, d) HAADF images showing segregation along grain

boundaries with different grain sizes

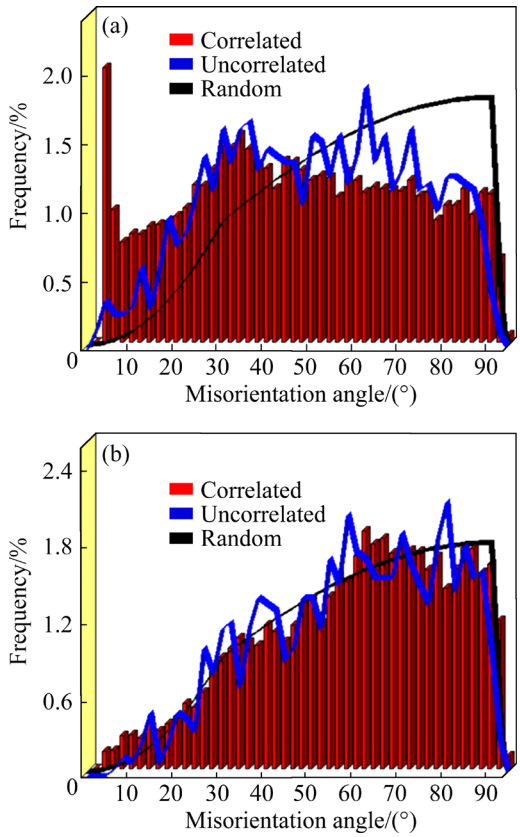

Fig. 12 Correlated and uncorrelated grain boundary misorientation distributions along with random uncorrelated distribution of RX region in as-extruded alloy (a) and 300 °C−10 h sample (b)

uncorrelated distribution (indicated by black lines) is also shown for comparison. For the RX region of the as-extruded alloy (Fig. 12(a)), it is seen that the frequency of uncorrelated misorientation angle (<45°) is higher than that of the random line, while lower than that of the random line at high misorientation angles (>60°). This difference is related to the formation of $\langle 01\bar{1}0\rangle$ texture. For 300 °C−10 h sample, the difference between the uncorrelated misorientation angle distribution and the random line is small, indicating that the texture is weak, which is consistent with the result shown in Fig. 10.

BHATTACHARYYA et al [45] reported that the $\langle \bar{1}2\bar{1}0\rangle$-oriented grains of a rolled AZ31 alloy grew up preferentially during annealing, resulting in a stronger $(0001)\langle \bar{1}2\bar{1}0\rangle$ texture in the annealed samples. An obvious peak of 30° was seen from the correlated misorientation angle distribution. The reason for the stronger $\langle \bar{1}2\bar{1}0\rangle$ texture was attributed to the low-energy 30° [0001] grain boundaries. In this work, the correlated misorientation angle distribution shows that no obvious peak can be observed in 300 °C−10 h sample (Fig. 12(b)). However, the frequency of boundaries with a higher misorientation angle (>60°) is greater than that of lower misorientation angles, indicating that higher misorientation angle exhibits a higher mobility. ZHANG et al [43] reported that TD-oriented grains had a higher frequency of higher misorientation angles, and boundaries with lower misorientation angles displayed higher concentrations of solute atoms and thus lower mobility. Some studies [44,45] reported that annealed Mg alloys showed a relatively high frequency of LAGBs. LAGBs exhibit low mobility, which can impede the grain growth [45]. However, as shown in Fig. 12(b), 300 °C−10 h sample shows a low proportion of LAGBs. Therefore, it can be inferred that LAGBs have little effect on inhibiting the grain growth of 300 °C−10 h sample.

Curvature-driven grain growth mechanism is also used to explain the preferential grain growth [41,46]. In Fig. 10(a), some abnormally coarse grains without $\langle 01\bar{1}0\rangle$ orientations can be observed. Coarse grains have a tendency to incorporate smaller grains, aiming to minimize the total grain boundary area and, consequently, reduce grain boundary energy [41]. Therefore, the growth of these coarse grains can be driven by the curvatures of grain boundaries, thereby continuously consuming surrounding grains.

5 Conclusions

(1) Annealing promoted the occurrence of SRX in the low-temperature extruded alloy. Compared with 200 and 250 °C, annealing at 300 °C not only accelerated the RX process, but also led to a rapid grain growth. The intermediate annealing temperature of 250 °C was beneficial for controlling the RX fraction and attaining fine-grained microstructure.

(2) With increasing annealing temperature, the Avrami exponent increased from ~0.37 to ~0.80. The activation energy for grain growth was determined to be ~153 kJ/mol. The high grain growth activation energy was related to the strong Zener pinning or drag force caused by grain boundary segregation.

(3) After annealing at 300 °C for 10 h, the texture component $\langle 01\bar{1}0\rangle$//ED in the as-extruded alloy was fully transformed into other four new texture components, including $\langle 20\bar{2}1\rangle$, $\langle 20\bar{2}3\rangle$, $\langle \bar{1}2\bar{1}2\rangle$ and $\langle \bar{2}7\bar{5}0\rangle$. Preferential grain growth was the main reason to the texture evolution, which was primarily affected by the strain energy difference and grain boundary segregation.

CRediT authorship contribution statement

Hua WANG: Conceptualization, Methodology, Investigation, Data curation, Writing − Original draft; **Da-tong ZHANG:** Supervision, Resources, Investigation, Writing − Review & editing; **Cheng QIU:** Software, Methodology; **Dao-lun CHEN:** Supervision, Resources, Investigation, Writing − Review & editing.

Declaration of competing interest

The authors declare that they have no known competing financial interests or personal relationships that could have appeared to influence the work reported in this paper.

Acknowledgments

This work was sponsored by the Key-Area Research and Development Program of Guangdong Province, China (No. 2020B010186002), the Natural Science Foundation of Guangdong for Research Team, China (No. 2015A030312003), and National Study Abroad Fund. D. L. CHEN is also grateful for the financial support by Natural Sciences and Engineering Research Council of Canada (NSERC). The authors would also like to thank S S DASH, D BAJAJ, Q LI, C MA, A MACHIN and J SCHWARTZ for their assistance and easy access to the laboratory facilities of Toronto Metropolitan University and their assistance in the experiments.

References

[1] YANG Y, XIONG X M, CHEN J, PENG X D, CHEN D L, PAN F S. Research advances of magnesium and magnesium alloys worldwide in 2022 [J]. Journal of Magnesium and Alloys, 2023, 11: 2611−2654.

[2] SHIRI M, JAFARI H, SINGH R. Effect of extrusion parameters on degradation of magnesium alloys for bioimplant applications: A review [J]. Transactions of Nonferrous Metals Society of China, 2022, 32: 2787−2813.

[3] ZHANG Z, ZHANG J H, XIE J S, LIU S J, HE Y Y, GUAN K, WU R Z. Developing a low-alloyed fine-grained Mg alloy with high strength−ductility based on dislocation evolution and grain boundary segregation [J]. Scripta Materialia, 2022, 209: 114414.

[4] ZHENG L W, ZHUANG Y P, LI J J, WANG H X, LI H, HOU H, WANG L F, LUO X P, SHIN K S. Mechanical properties of Mg−Gd−Zr alloy by Nd addition combined with hot extrusion [J]. Transactions of Nonferrous Metals Society of China, 2022, 32: 1866−1880.

[5] LIU S S, LIU H, ZHANG B X, HUANG G S, CHEN X, TANG A T, JIANG B, PAN F S. Effects of extrusion temperature on microstructure evolution and mechanical properties of heterogeneous Mg−Gd alloy laminates via accumulated extrusion bonding [J]. Transactions of Nonferrous Metals Society of China, 2022, 32: 2190−2204.

[6] FAN W X, BAI Y, LI G Y, CHANG X Y, HAO H. Enhanced mechanical properties and formability of hot-rolled Mg−Zn−Mn alloy by Ca and Sm alloying [J]. Transactions of Nonferrous Metals Society of China, 2022, 32: 1119−1132.

[7] SUH B C, SHIM M S, SHIN K S, KIM N J. Current issues in magnesium sheet alloys: Where do we go from here? [J]. Scripta Materialia, 2014, 84/85: 1−6.

[8] WANG H, ZHANG D T, CAO G H, QIU C. Improving room-temperature ductility of a Mg−Zn−Ca alloy through friction stir processing [J]. Journal of Materials Research and Technology, 2022, 17: 1176−1186.

[9] LI L, ZHANG C C, LV H, LIU C R, WEN Z Z, JIANG J W. Texture development and tensile properties of Mg−Yb binary alloys during hot extrusion and subsequent annealing [J]. Journal of Magnesium and Alloys, 2022, 10: 249−265.

[10] MD F K, KARTHIK G M, PANIGRAHI S K, JANAKI RAM G D. Friction stir processing of QE22 magnesium alloy to achieve ultrafine-grained microstructure with enhanced room temperature ductility and texture weakening [J]. Materials Characterization, 2019, 147: 365−378.

[11] CHINO Y, UEDA T, OTOMATSU Y, SASSA K, HUANG X S, SUZUKI K, MABUCHI M. Effects of Ca on tensile properties and stretch formability at room temperature in Mg−Zn and Mg−Al alloys [J]. Materials Transactions, 2011, 52: 1477−1482.

[12] GUAN D K, LIU X G, GAO J H, MA L, WYNNE B P, RAINFORTH W M. Exploring the mechanism of “Rare Earth” texture evolution in a lean Mg−Zn−Ca alloy [J]. Scientific Reports, 2019, 9: 7152.

[13] CANO-CASTILLO G, VICTORIA-HERNÁNDEZ J, BOHLEN J, LETZIG D, KAINER K U. Effect of Ca and Nd on the microstructural development during dynamic and static recrystallization of indirectly extruded Mg−Zn based alloys [J]. Materials Science and Engineering: A, 2020, 793: 139527.

[14] DING P F, LIU Y C, HE X H, LIU D B, CHEN M F. In vitro and in vivo biocompatibility of Mg−Zn−Ca alloy operative clip [J]. Bioactive Materials, 2019, 4: 236−244.

[15] DU S, YANG K, LI M, LI J R, REN Y P, HUANG Q Y, PAN H C, QIN G W. Achieving high strength above 400 MPa in conventionally extruded Mg−Ca−Zn ternary alloys [J]. Science China Technological Sciences, 2022, 65: 519−528.

[16] WANG Q H, ZHAI H W, WANG L, XU J, CHEN Y, JIANG B. A new strong and ductile multicomponent rare-earth free

Mg−Bi-based alloy achieved by extrusion and subsequent short-term annealing [J]. Materials Science and Engineering: A, 2022, 860: 144309.

[17] WU X F, XU C X, ZHANG Z W, YANG W F, ZHANG J S. Microstructure evolution, strengthening mechanisms and deformation behavior of high-ductility Mg−3Zn−1Y−1Mn alloy at different extrusion temperatures [J]. Transactions of Nonferrous Metals Society of China, 2023, 33: 422−437.

[18] WU W X, JIN L, ZHANG Z Y, DING W J, DONG J. Grain growth and texture evolution during annealing in an indirect-extruded Mg−1Gd alloy [J]. Journal of Alloys and Compounds, 2014, 585: 111−119.

[19] LU X, ZHAO G Q, ZHOU J X, ZHANG C S, CHEN L, TANG S Q. Microstructure and mechanical properties of Mg−3.0Zn−1.0Sn−0.3Mn−0.3Ca alloy extruded at different temperatures [J]. Journal of Alloys and Compounds, 2018, 732: 257−269.

[20] STANFORD N, BARNETT M R. The origin of “rare earth” texture development in extruded Mg-based alloys and its effect on tensile ductility [J]. Materials Science and Engineering: A, 2008, 496: 399−408.

[21] HUANG G H, YIN D D, LU J W, ZHOU H, ZENG Y, QUAN G F, WANG Q D. Microstructure, texture and mechanical properties evolution of extruded fine-grained Mg−Y sheets during annealing [J]. Materials Science and Engineering: A, 2018, 720: 24−35.

[22] WANG H, ZHANG D T, QIU C, ZHANG W W, CHEN D L. Achieving superior mechanical properties in a low-alloyed magnesium alloy via low-temperature extrusion [J]. Materials Science and Engineering: A, 2022, 851: 143611.

[23] ALIZADEH R, MAHMUDI R, NGAN A H W, LANGDON T G. Microstructural stability and grain growth kinetics in an extruded fine-grained Mg−Gd−Y−Zr alloy [J]. Journal of Materials Science, 2015, 50: 4940−4951.

[24] HU G W, ZENG L C, DU H, WANG Q, FAN Z T, LIU X W. Combined effects of solute drag and Zener pinning on grain growth of a NiCoCr medium-entropy alloy [J]. Intermetallics, 2021, 136: 107271.

[25] WEYGAND D, BRÉCHET Y, LÉPINOUX J. Zener pinning and grain growth: A two-dimensional vertex computer simulation [J]. Acta Materialia, 1999, 47: 961−970.

[26] WANG Q H, JIANG B, TANG A T, FU J, JIANG Z T, SHENG H R, ZHANG D F, HUANG G S, PAN F S. Unveiling annealing texture formation and static recrystallization kinetics of hot-rolled Mg−Al−Zn−Mn−Ca alloy [J]. Journal of Materials Science & Technology, 2020, 43: 104−118.

[27] ZHANG Y, JIANG H T, WANG Y J, XU Z. Effects of second-phase particles on microstructure evolution in Mg−2Zn based magnesium alloys during annealing treatment [J]. Metals, 2020, 10: 777.

[28] PATEL V K, BHOLE S D, CHEN D L. Influence of ultrasonic spot welding on microstructure in a magnesium alloy [J]. Scripta Materialia, 2011, 65: 911−914.

[29] LIU S S, CHEN Y F, YANG H, HUANG G S, CHEN X H, TANG A T, JIANG B, PAN F S. Revealing the role of heterostructural parameters in hetero-deformation induced stress of Mg−13Gd alloy [J]. Materials Science and Engineering: A, 2022, 839: 142844.

[30] MINÁRIK P, KRÁL R, ČÍŽEK J, CHMELÍK F. Effect of different *c*/*a* ratio on the microstructure and mechanical properties in magnesium alloys processed by ECAP [J]. Acta Materialia, 2016, 107: 83−95.

[31] ZHAO L Y, GUAN B, XIN Y C, HUANG X X, LIU C L, WU P D, LIU Q. A quantitative study on mechanical behavior of Mg alloys with bimodal texture components [J]. Acta Materialia, 2021, 214: 117013.

[32] AVRAMI M. Granulation, phase change, and microstructure kinetics of phase change. III [J]. The Journal of Chemical Physics, 1941, 9: 177−184.

[33] CHAO H Y, SUN H F, CHEN W Z, WANG E D. Static recrystallization kinetics of a heavily cold drawn AZ31 magnesium alloy under annealing treatment [J]. Materials Characterization, 2011, 62: 312−320.

[34] SU C W, LU L, LAI M O. Recrystallization and grain growth of deformed magnesium alloy [J]. Philosophical Magazine, 2008, 88: 181−200.

[35] JIANG M G, XU C, YAN H, NAKATA T, CHEN Z W, LAO C S, CHEN R S, KAMADO S, HAN E H. Quasi-in-situ observing the rare earth texture evolution in an extruded Mg−Zn−Gd alloy with bimodal microstructure [J]. Journal of Magnesium and Alloys, 2021, 9: 1797−1805.

[36] BURKE J E, TURNBULL D. Recrystallization and grain growth [J]. Progress in Metal Physics, 1952, 3: 220−292.

[37] PEI R S, ZOU Y C, ZUBAIR M, WEI D Q, AL-SAMMAN T. Synergistic effect of Y and Ca addition on the texture modification in AZ31B magnesium alloy [J]. Acta Materialia, 2022, 233: 117990.

[38] YU H H, XIN Y C, WANG M Y, LIU Q. Hall−Petch relationship in Mg alloys: A review [J]. Journal of Materials Science & Technology, 2018, 34: 248−256.

[39] ZENG Z R, ZHU Y M, XU S W, BIAN M Z, DAVIES C H J, BIRBILIS N, NIE J F. Texture evolution during static recrystallization of cold-rolled magnesium alloys [J]. Acta Materialia, 2016, 105: 479−494.

[40] WANG H, ZHANG D T, QIU C, ZHANG W W, CHEN D L. Achieving superior strength−ductility synergy in a heterostructured magnesium alloy via low-temperature extrusion and low-temperature annealing [J]. Journal of Materials Science & Technology, 2023, 163: 32−44.

[41] LIU H Y, ZHU S M, ABBOTT T B, ZHEN Z S, NIE J F. Quasi-in-situ EBSD study of the microstructure and texture evolution during static recrystallization in an extruded Mg−Mn−Ce Alloy [J]. JOM, 2022, 74: 2592−2608.

[42] VICTORIA-HERNÁNDEZ J, SUH J, YI S, BOHLEN J, VOLK W, LETZIG D. Strain-induced selective grain growth in AZ31 Mg alloy sheet deformed by equal channel angular pressing [J]. Materials Characterization, 2016, 113: 98−107.

[43] ZHANG M N, JIA H L, ZHA M, ZHAO L, HUA Z M, WANG C, GAO Y P, WANG H Y. Anisotropic segregation-driven texture weakening in a dilute Mg−Al−Ca alloy during isothermal annealing [J]. Materials Research Letters, 2023, 11: 781−788.

[44] ZHAO L Y, YAN H, CHEN R S, HAN E H. Study on the evolution pattern of grain orientation and misorientation during the static recrystallization of cold-rolled Mg−Zn−Gd

alloy [J]. Materials Characterization, 2019, 150: 252−266.
[45] BHATTACHARYYA J J, AGNEW S R, MURALIDHARAN G. Texture enhancement during grain growth of magnesium alloy AZ31B [J]. Acta Materialia, 2015, 86: 80−94.
[46] IMANDOUST A, BARRETT C D, OPPEDAL A L, WHITTINGTON W R, PAUDEL Y, EL KADIRI H. Nucleation and preferential growth mechanism of recrystallization texture in high purity binary magnesium−rare earth alloys [J]. Acta Materialia, 2017, 138: 27−41.

低温挤压 Mg−Zn−Ca 合金在退火过程中的静态再结晶动力学和织构演变

王 华[1,2]，张大童[1]，邱 诚[1]，陈道伦[2]

1. 华南理工大学 国家金属材料近净成形工程技术研究中心，
广东省金属新材料制备与成形重点实验室，广州 510640；
2. Department of Mechanical, Industrial and Mechatronics Engineering, Toronto Metropolitan University, Toronto, Ontario M5B 2K3, Canada

摘 要：在 150 ℃对低合金含量 Mg−1.2Zn−0.1Ca 合金进行挤压，随后在 200~300 ℃之间进行退火处理，对材料的显微组织演变和静态再结晶动力学进行研究。挤压态合金为细小的再结晶晶粒(0.8 μm)和粗大的非再结晶晶粒组成的双峰结构，再结晶分数约为 67%。退火温度 250 ℃的再结晶速率适中，再结晶晶粒生长速率较慢。$\langle 20\bar{2}1\rangle$、$\langle 20\bar{2}3\rangle$、$\langle \bar{1}2\,\bar{1}2\rangle$和$\langle \bar{2}7\bar{5}0\rangle$取向的晶粒在长时间退火过程中表现出择优长大的优势。晶界偏析对晶界产生强烈的 Znner 钉扎效应，不仅增加了晶粒长大激活能，而且影响了织构演变。

关键词：Mg−Zn−Ca 合金；退火；织构；晶粒长大；静态再结晶动力学

(Edited by Xiang-qun LI)